Computer Model Calibration with Large Spatial Outputs

Kai-Lan Chang and Serge Guillas*
University College London
ucakkac@ucl.ac.uk

Abstract

The Bayesian computer model calibration method has proven to be effective in a wide range of applications. In this framework, input parameters are tuned by comparing model outputs to observations. However, this methodology becomes computationally expensive for large spatial model outputs. To overcome this challenge, we employ a truncated basis representations of the model outputs. We then aim to match the model outputs coefficients with the coefficients from observations in the same basis; we also optimize the truncation level. In a second step, we enhance the calibration with the addition of the INLA-SPDE technique. We embed nonstationary behavior and derivative information of the spatial field into the calibration by inserting two INLA-SPDE parameters into the calibration. Several synthetic examples and a climate model illustration highlight the benefits of our approach for model outputs distributed over the plane or the sphere.

Keywords: dimension reduction; SPDE; Matérn fields; uncertainty quantification

1 Introduction

Complex computer models are widely used in various fields of science and technology to mimic complex physical systems. Computer model calibration involves comparing the simulations of a complex computer model with the physical observations of the process being simulated. Increasingly, computer model outputs are in the form of spatial fields, particularly in environmental sciences. This poses a particular challenge to the calibration method. In this paper we develop our Bayesian calibration technique based on the framework from Kennedy and O'Hagan (2001): we approximate the expensive computer model by a Gaussian process (GP). This formulation has proven to be effective in a wide range of applications. However, the GP calibration is computationally expensive for large model input and output spaces (typically cubic in the number of data points used to fit the GP). Therefore several attempts to tackle this issue have been made by using truncated basis representations of model outputs in order to reduce dimension (Bayarri et al., 2007; Higdon et al., 2008; Chang et al., 2014).

Gaussian fields (GF) play an important role in spatial statistics and form a major area of interest within the field of Bayesian hierarchical spatial models. The traditional approach is to specify a GF through its covariance function. Another approach is to use the class of Gaussian Markov random fields (GMRF), which are discretely indexed GFs. The Markov property yields a sparse precision matrix, so that efficient numerical algorithms can be employed. Lindgren et al. (2011) show that the GMRF representation can be constructed explicitly by using a certain form of stochastic partial differential equation (SPDE) which has a GF with Matérn covariance function as its solution when driven by Gaussian white noise. The representation employs piecewise linear basis functions, and Gaussian weights with Markov dependences determined by the finite element method over a triangulation of the domain. This technique can deal with

*Kai-Lan Chang was supported by the Taiwanese government sponsorship for Ph.D. overseas study. S. Guillas was partially supported by a Leverhulme Trust research fellowship on "stratospheric ozone and climate change" (RF/9/RFG/2010/0427). We also thank Hanli Liu (NCAR) for technical support in running the chemistry-climate model WACCM.

large spatial data sets and naturally account for nonstationarity. Our paper extends both the calibration formulation and the SPDE defined scale and precision parameters to fit large scale spatial outputs, and still provides a compromise with computational feasibility in order to employ a fully Bayesian approach.

Our main motivation is the calibration of computer models with spatial outputs. To describe the general framework in spatial modeling, let $\boldsymbol{\eta}(\mathbf{s}_i, \boldsymbol{\theta}_j), i = 1, \ldots, n; j = 1, \ldots, r$ be the r-runs model output measured at n locations. Here we refer to $m = n \times r$ as the total number of outputs in the simulations. We choose a design made of combinations of parameter values, and we impose distributional prior assumptions on the calibration parameters $\boldsymbol{\theta}$. The aim of calibration is to compare with observations and estimate the best input setting $\boldsymbol{\theta}^*$. Computer model calibration is a computationally expensive procedure, and is often infeasible even for moderately large computer model outputs, such as climate or chemistry–transport modeling. Every computer experiment may produce $n > 10,000$ high resolution spatial outputs. Computer model experiments involve a design of runs to explore the behavior of the computer model over a region of the input space, typically at least 10 runs per parameters. The resulting number of simulations m, combined with the output dimension n may become too large to fit GPs to the computer model and the discrepancy between model and observations and thus may prevent the fully Bayesian calibration to be performed.

The aim of this article is to develop a method to calibrate numerical models with large spatial outputs, particularly on the sphere. We employ a truncated basis representation, such as B–splines decompositions, Fourier transforms or spherical harmonics, to capture the output features spatially. In Section 2.1 we present our approach. We then explore how parameters in an SPDE model can explicitly quantify the nonstationarity and derivative information the spatial field (Bolin and Lindgren, 2011; Zammit-Mangion et al., 2015). Hence in Section 2.2 we extend our approach by including the basis representation of the scale and precision parameters in an SPDE model into our calibration framework. In Section 3, we apply these techniques to different synthetic examples and a real computer experiment, with the aim of evaluating performance of our calibration method under different sources of uncertainty. Finally in Section 4, we discuss potential improvements to our approach.

2 Methods

2.1 Basis representation for the model output

In this section, we derive a basis representation for the model output $\boldsymbol{\eta}$ and field observations y^F with the real valued basis functions $\{\psi_z\}, z = 1, \ldots, N$, such as B–spline, spherical harmonics (SHs), or some other basese, to represent the surfaces produced by computer models and observations, and construct a methodology for the calibration employing the coefficients in these representations. The observed surface data $y^F(\mathbf{s})$ are collected at a number of location inputs $\mathbf{s}$ in an n-point spatial data D^F. Let $\boldsymbol{\theta}$ be the calibration inputs used to infer the best combination of inputs $\boldsymbol{\theta}^*$. The model output $\boldsymbol{\eta}(\cdot)$ is running at inputs $(\mathbf{s}, \boldsymbol{\theta})$ in an m-point design D^M, where $m = n \times r$ means r computer runs measured at n locations. Then we can use the same basis functions $\{\psi_z\}$ to decompose each computer output, i.e., for the N-th order expansion and for each run j:

$$\boldsymbol{\eta}(\mathbf{s}, \boldsymbol{\theta}_j) = \sum_{z=0}^{N} c_{z,j}^M(\boldsymbol{\theta}_j)\psi_z(\mathbf{s}) + \varepsilon_N, \qquad j = 1, \ldots, r,$$

where ε_N is an error term associated with the order N. The coefficients $\{c^M\}$ represent the large-scale surface or curve features at different resolutions. This transformation separates the

spatial effect from the variations triggered by the calibration inputs $\boldsymbol{\theta}$. To exploit the information of the calibration parameters, we translate the variations in $\boldsymbol{\theta}$ only into the expanded coefficients.

Similarly, the observed field surface can be written as

$$y^F(\mathbf{s}) = \sum_{z=1}^{N} c_z^F \psi_z(\mathbf{s}).$$

By applying a basis representation, the physical space of both model outputs and field data are transformed into a functional space. Since the aim is to calibrate the spatial process on the sphere, we also assume that the real physical process $y^R(\mathbf{s})$, the discrepancy function $\delta(\mathbf{s})$ between reality and the computer model, and the measurement errors $\epsilon(\mathbf{s})$, can be accurately represented by the same basis functions:

$$y^R(\mathbf{s}) = \sum_{z=1}^{N} c_z^R \psi_z(\mathbf{s}), \qquad \delta(\mathbf{s}) = \sum_{z=1}^{N} c_z^\delta \psi_z(\mathbf{s}), \qquad \epsilon(\mathbf{s}) = \sum_{z=1}^{N} c_z^\epsilon \psi_z(\mathbf{s}).$$

Then matching the coefficients yields

$$c_z^R = c_z^M(\boldsymbol{\theta}^*) + c_z^\delta, \qquad c_z^F = c_z^R + c_z^\epsilon, \qquad z = 1, \ldots, N.$$

The measurement errors in the functional space, c_z^ϵ, are assumed normally distributed with 0 mean and variance σ_z^2, and independent across z. The coefficients c_z^M can be assumed to have mean 0 with marginal variance close to 1 without loss of generality if the responses are standardized. The GP assumption can be imposed on each coefficient $c_z^M(\boldsymbol{\theta}), z = 1, \ldots, N$, of mean 0 and with covariance function

$$\mathrm{Cov}(\boldsymbol{\theta}, \boldsymbol{\theta}') = \frac{1}{\lambda_\eta} I_{zz'} \prod_{k=1}^{q} \rho_{\eta k}^{4(\theta_k - \theta_k')^2}, \tag{1}$$

where $I_{zz'}$ is the Kronecker's delta ($I_{zz'} = 1$ if $z = z'$ and 0 otherwise), q is the dimension of $\boldsymbol{\theta}$, λ_η controls the marginal precision of $\boldsymbol{\eta}(\cdot, \cdot)$ and $\boldsymbol{\rho}_\eta$ controls the strength of the dependence in each of the pairs of $\boldsymbol{\theta}$. This formulation leads to a smooth and infinitely differentiable representation for the model output. We also assume that the correlation between different categories i of the coefficients is 0 (see later discussion). Hence the rN-vector $\mathbf{c}^M$ has a multivariate normal prior with mean 0 and a block diagonal covariance matrix. The specifications for λ_η and $\boldsymbol{\rho}_\eta$ are gamma priors and independent beta priors: $\pi(\lambda_\eta) \sim \lambda_\eta^{a_\eta - 1} e^{-b_\eta \lambda_\eta}$ and $\pi(\rho_{\eta k}) \sim \rho_{\eta k}^{a_{\rho_\eta} - 1}(1 - \rho_{\eta k})^{b_{\rho_\eta} - 1}, k = 1, \ldots, q$.

The discrepancy term c_z^δ quantifies the inadequacy (also called discrepancy) between the simulator and reality in the functional domain, which is independent of the c_z^M. We assume that c_z^δ follows a GP model:

$$c_z^\delta \sim N\left(\mathbf{0}, \frac{1}{\lambda_\delta} I_{zz'}\right). \tag{2}$$

This assumption required careful handling as there may not be enough degrees of freedom in the truncated basis to capture all of the variability. The prior specification for the parameter λ_δ is a gamma prior $\pi(\lambda_\delta) \sim \lambda_\delta^{a_\delta - 1} e^{-b_\delta \lambda_\delta}$.

Denote the joint $(r+1)N$ data vector $\mathbf{d} = (c^F, c^M)$. The sampling likelihood for the full data is then

$$L(\mathbf{d}|\boldsymbol{\theta}^*, \lambda_\eta, \boldsymbol{\rho}_\eta, \lambda_\delta, \Sigma_y) \propto |\Sigma_\mathbf{d}|^{-1/2} \exp\left\{-\frac{1}{2}(\mathbf{d}^T \Sigma_\mathbf{d}^{-1} \mathbf{d})\right\}, \tag{3}$$

where

$$\Sigma_{\mathbf{d}} = \Sigma_\eta + \begin{pmatrix} \Sigma_y + \Sigma_\delta & 0 \\ 0 & 0 \end{pmatrix},$$

in which Σ_y is the $N \times N$ observation covariance matrix, Σ_η is obtained for each pair of $(r+1)N$ simulation inputs through (1) corresponding to $\mathbf{d}$, and Σ_δ is an $N \times N$ matrix obtained for each pair of N input through the instances of (2) that correspond to the coefficients c^F.

Let $\pi(\boldsymbol{\theta}^*)$ be the joint prior distribution for the calibration value, evaluated at the (unknown) best calibration value $\boldsymbol{\theta}^*$. The resulting posterior density has the form

$$\pi(\boldsymbol{\theta}^*, \lambda_\eta, \boldsymbol{\rho}_\eta, \lambda_\delta | \mathbf{d}) \propto L(\mathbf{d}|\boldsymbol{\theta}^*, \lambda_\eta, \boldsymbol{\rho}_\eta, \lambda_\delta) \times \pi(\boldsymbol{\theta}^*) \times \pi(\lambda_\eta) \times \pi(\boldsymbol{\rho}_\eta) \times \pi(\lambda_\delta), \tag{4}$$

which can be explored via a Markov chain Monte Carlo (MCMC) technique, for which we employ a Metropolis–Hastings algorithm.

The strong assumption of independence of the coefficients with different categories may not be fully justifiable in real applications. However, this assumption leads to a great computational advantage in terms of forming a block diagonal covariance model in the GP model. In section 3 we discuss how this assumption is a compromise between fidelity and complexity. The other treatment of such categorical parameter can be found by Storlie et al. (2015). Furthermore, it is not general knowledge to know how to specify the covariance structures for the truncated basis representation due to the mathematical challenge of finding explicit expressions for the covariance (Jun and Stein, 2008). Nevertheless, there is an alternative way to include a nonstationary structure into our calibration algorithm. We introduce it in the next section.

2.2 Calibration with SPDE model parameters

The Matérn covariance function is an advanced covariance structure used to model dependence of spatial data on the plane. The shape parameter ν, the scale parameter κ, and the marginal precision τ^2, parameterize it:

$$C(\mathbf{h}) = \frac{2^{1-\nu}}{(4\pi)^{d/2}\Gamma(\nu + d/2)\kappa^{2\nu}\tau^2}(\kappa\|\mathbf{h}\|)^\nu K_\nu(\kappa\|\mathbf{h}\|), \mathbf{h} \in \mathbb{R}^d, \tag{5}$$

where $\mathbf{h}$ denotes the difference between any two locations s and s': $\mathbf{h} = s - s'$, and K_ν is the modified Bessel function of the second kind of order $\nu > 0$.

We denote by $Y(\mathbf{s})$ the spatial measurements or computer model outputs for a latent spatial field $X(\mathbf{s})$, for which we assume a zero mean Gaussian noise, $\mathcal{W}(\mathbf{s})$, with a constant variance σ_s^2: $Y(\mathbf{s}) = X(\mathbf{s}) + \mathcal{W}(\mathbf{s})$. Thus, according to Whittle (1963), the covariance structure of the latent field $X(\mathbf{s})$ can be generated by an SPDE:

$$(\kappa^2(\mathbf{s}) - \Delta)^{\alpha/2}\tau(s)X(\mathbf{s}) = \mathcal{W}(\mathbf{s}). \tag{6}$$

The solution to the SPDE is a Gaussian random field with Matérn covariance structure. The regularity (or smoothness) parameter ν essentially determines the order of differentiability of the fields. The link between the Matérn field and the SPDE is given by $\alpha = \nu + d/2$, which makes explicit the relationship between dimension and regularity for fixed α. On more general manifolds than $\mathbb{R}^d$, the direct Matérn representation is not easy to implement, but the SPDE formulation provides a natural generalization, and the ν-parameter will keep its meaning as the quantitative measure of regularity. Instead of defining Matérn fields by the covariance function, Lindgren et al. (2011) used the solution of the SPDE as a definition, and it is much easier and flexible to do so. This definition works not only on $\mathbb{R}^d$ but also on general smooth manifolds, such as on the sphere, and facilitates nonstationary extensions by allowing the SPDE parameters κ and τ to vary with space.

The field $X(\mathbf{s})$ can be built on a basis representation: $X(\mathbf{s}) = \sum_{i=1}^{M} \varphi_i(\mathbf{s}) w_i$, where the w_i is the stochastic weight chosen so that the $X(\mathbf{s})$ approximates the distribution of solutions to the SPDE on a space. The basis functions $\varphi_i(\mathbf{s})$ are chosen by a finite element method in order to obtain a Markov structure, and to preserve it when conditioning on local observations. To allow an explicit expression of the precision matrix for the stochastic weights, we use a piecewise linear basis functions for the location of the observations. Let $\mathbf{C} = \langle \varphi_i, \varphi_{i'} \rangle$ and $\mathbf{G} = \langle \nabla \varphi_i, \nabla \varphi_{i'} \rangle$ be matrices used in the construction of the finite element solutions of the SPDE approach. For $\alpha = 2$, the precision matrix for the weights $\{w_i\}$ is given by $\mathbf{Q} = \tau^2(\kappa^4\mathbf{C} + 2\kappa^2\mathbf{G} + \mathbf{G}\mathbf{C}^{-1}\mathbf{G})$, where the elements of $\mathbf{Q}$ have explicit expressions as functions of κ and τ (Lindgren et al., 2011). Note that the SPDE model is constructed through this triangular mesh. The mesh can be more adaptive and flexible to irregularly distributed spatial observations.

As discussed in Jun and Stein (2008), the mean structure of a spatial process can be modeled using a regression basis of eigenfunctions. However, since the datasets often only contain measurements from one specific event, it is not possible to identify which part of the variation in the data comes from a varying mean and which part can be explained by the variance–covariance structure of the latent field (Bolin and Lindgren, 2011). Let $\kappa(\mathbf{s}, \boldsymbol{\theta})$ and $\tau(\mathbf{s}, \boldsymbol{\theta})$ be the scale and precision parameters in an SPDE model used to approximate computer model outputs. To obtain basic identifiability, $\kappa(\mathbf{s}, \boldsymbol{\theta})$ and $\tau(\mathbf{s}, \boldsymbol{\theta})$ are taken to be positive, and their logarithm can be decomposed as (in N-th order decomposition):

$$\log \kappa(\mathbf{s}, \boldsymbol{\theta}) = \sum_{z=0}^{N} \kappa_z(\boldsymbol{\theta}) \psi_z(\mathbf{s}), \quad \log \tau(\mathbf{s}, \boldsymbol{\theta}) = \sum_{z=0}^{N} \tau_z(\boldsymbol{\theta}) \psi_z(\mathbf{s}).$$

The parameter $\kappa(\mathbf{s}, \boldsymbol{\theta})$ directly controls the (local) spatial range and measures how rapidly the correlation of the random field decays with distance, with smaller value corresponding to a slower decay (keeping other parameters fixed), and $\tau(\mathbf{s}, \boldsymbol{\theta})$ measures the marginal precision over the process: a small value means higher marginal variance.

We estimate the SPDE parameters and supply uncertainty information about the surfaces by using the *integrated nested Laplacian approximations* (INLA) framework, available as an R package (`http://www.r-inla.org/`). The default value in R-INLA is $\alpha = 2$, but $0 \leq \alpha < 2$ are also available, though yet to be completely tested (Lindgren and Rue, 2015). So with $\alpha = 2$ and a 2-manifold (both in $\mathbb{R}^2$ and $\mathbb{S}^2$), the smoothness parameter ν must be fixed at 1 due to the relationship $\alpha = \nu + d/2$. For the prior specifications of the SPDE, κ and τ follow log normal priors by default: median for τ (prior.variance.nominal) = 1 and median for κ (prior.range.nominal) depends on the mesh. We use a regression basis of B–splines or SHs for both of these parameters; therefore by default the coefficients follow the log normal priors. We do not change the R–INLA default prior settings throughout the analysis.

As $\kappa(\mathbf{s}, \boldsymbol{\theta})$ and $\tau(\mathbf{s}, \boldsymbol{\theta})$ can capture the nonstationarity and derivative information in the spatial process, we now include these two coefficients into our technique. Let $\{\kappa_z^F, \tau_z^F\}$ be the coefficients in the SPDE parameters for the observations, and $\{\kappa_{z,j}^M, \tau_{z,j}^M\}$ be the coefficients estimated by the SPDE for computer run j in associated with model discrepancy presented. Then observations consist of the coefficients $\{c_z^F, \kappa_z^F, \tau_z^F\}$, and model outputs consist of the coefficients $\{c_{z,j}^M, \kappa_{z,j}^M, \tau_{z,j}^M\}, j = 1, \ldots, r$.

The aim is to combine the scale and precision parameters as nonstationary covariance information for the implementation of the calibration algorithm, and to model all coefficients jointly with the GP assumption. The expansion order of the basis functions for $\{c_{z,j}^M, \kappa_{z,j}^M, \tau_{z,j}^M\}$, do not need to be the same, and coefficients with different categories i are treated as independent. We also assume that the three types of coefficients are independent. To describe the formulation of the design matrix, let $\{z_1, z_2, z_3 | z_1 = 1, \ldots, N_\eta; z_2 = 1, \ldots, N_\kappa; z_3 = 1, \ldots, N_\tau\}$ be the number of coefficients used to represent each triplet of coefficients, respectively. Thus there are $(N_\eta + N_\kappa + N_\tau)$-categorical coefficients corresponding to each combination of $\boldsymbol{\theta}_j, j = 1 \ldots, r$ in the design matrix. The total size of design matrix for the computer model is $r(N_\eta + N_\kappa + N_\tau) \times$

$(1+q)$. The GP assumption is imposed on each coefficient $\{c^M_{z_1,j}, \kappa^M_{z_2,j}, \tau^M_{z_3,j}\}$ with mean 0 and covariance function

$$\text{Cov}((\mathbf{z},\boldsymbol{\theta}),(\mathbf{z}',\boldsymbol{\theta}')) = \frac{1}{\lambda_\eta}\prod_{i=1}^{3} I_{z_i z_i'} \prod_{k=1}^{q} \rho_{\eta k}^{4(\theta_k-\theta_k')^2}.$$

Hence the $r(N_\eta + N_\kappa + N_\tau)$-vector $\{\mathbf{c}^M_{z_1}, \boldsymbol{\kappa}^M_{z_2}, \boldsymbol{\tau}^M_{z_3}\}$ has a multivariate normal prior distribution with mean 0 and the covariance structure forms a block diagonal matrix.

As we assumed independence between different categories of coefficients, the model discrepancy term in the functional space follows a GP assumption defined in Equation (2). All the prior assumptions discussed in the previous section remain unchanged. Thus the sampling likelihood in (3) and the posterior distribution in (4) still hold in this case. Overall, we decompose the model outputs into a basis of eigenfunctions via the coefficients c^M, and estimate the SPDE parameters $\{\kappa^M, \tau^M\}$ in the latent field through a regression onto the eigenfunctions. We are essentially inverse fitting a GP model with c^M for the regression mean structure and $\{\kappa^M, \tau^M\}$ for the Matérn covariance function (with ν fixed in connection with SPDE model).

3 Simulation Study and Application

In order to illustrate the methodology, we present four synthetic examples and one real computer experiment. In example 1, we start with a simulation over irregularly spaced outputs in $\mathbb{R}^2$ as it is less complex than in $\mathbb{S}^2$. Then we extend our technique step–by–step to a spherical output. Example 2 shows how the dimension reduction works from a spherical output to a spherical representation. We investigate the connection between the calibration accuracy and the number of computer runs r, and between the calibration accuracy and the orders/modes of SHs. Example 3 is designed to compare different basis representations for the model output, with the aim of evaluating the respective performances of the SHs approach and the principal components (PCs) approach (Higdon et al., 2008). Example 4 simulates a nonstationary field on the sphere, with an anisotropical property (the spatial correlation depends on latitude), to demonstrate how including the parameters in the SPDE can further benefit the GP calibration. Finally, in our application to real data, we perform the calibration of gravity wave (GW) parameters for the Whole Atmosphere Community Climate Model (WACCM) simulator, albeit with known synthetic observations (but with added nonstationary observation errors) in order to fully validate our approach.

3.1 Example 1: Irregular grids

To illustrate our methodology of dimension reduction for the spatial output, this example is devoted to a spatial calibration for irregularly spaced locations in $\mathbb{R}^2$. The true target function is a bivariate normal probability distribution function defined as

$$f(\mathbf{x},\boldsymbol{\theta}) = \frac{1}{2\pi\theta_1\theta_2}\exp\left(-\frac{1}{2\pi}\left(\frac{(x_1-0.5)^2}{\theta_1^2} - \frac{(x_1-0.5)(x_2-0.5)}{\theta_1\theta_2} + \frac{(x_2-0.5)^2}{\theta_2^2}\right)\right), \quad (7)$$

with the true values for (θ_1,θ_2) being set to (0.3, 0.7), and $\mathbf{x} = (x_1,x_2) \in [0,1]^2$. Both calibration and location parameters are generated by a maximin Latin hypercube design (LHD). We generated noisy observations of the field surface $y^F(\mathbf{x},\boldsymbol{\theta}^*) = f(\mathbf{x},\boldsymbol{\theta}^*) + \epsilon(\mathbf{x})$ at locations $(x_{1i},x_{2i}), i = 1,\ldots,100$, on an irregularly spaced grid, where $\epsilon(\mathbf{x}) \sim N(0,0.01)$. The model output $\eta(\mathbf{x},\boldsymbol{\theta}) = f(\mathbf{x},\boldsymbol{\theta}) + \delta(\mathbf{x})$ was generated employing the same 100 location inputs and 50 runs of a maximin LHD $\boldsymbol{\theta}_j = (\theta_{1j},\theta_{2j}), j = 1,\ldots,50$, where $\delta(\mathbf{x}) \sim N(\frac{1}{2}\sigma_y^2, 0.01)$, σ_y^2 is the

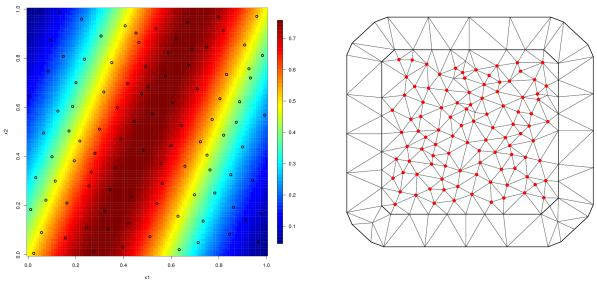

(a) Fields surface (b) Triangulation

Figure 1: (a) Fields surface with measured locations (circles); (b) Delaunay triangulation for SPDEs.

variance of the field data y^F. Figure 1(a) shows the distribution of the irregularly spaced grid (circles) in our design.

In order to investigate the benefit of incorporation of SPDE parameters into the calibration algorithm, the following models are compared: (1) Model A: 10 B–spline basis decomposition for η and y^F; (2) Model B: 15 B–spline basis decomposition for η and y^F; (3) Model C: 10 B–spline basis decomposition, including 2nd order B–spline for SPDE defined precision and scale parameters, for η and y^F. We represent the spatial field of the observations and each model output by the SPDE model, with the B–spline basis representation for the logarithms of κ and τ. The Delaunay triangular mesh for the SPDEs shown in Figure 1(b).

The specifications for the rest of hyperpriors are $\lambda_\epsilon \sim \Gamma(1, 10^{-5})$, $\lambda_\delta \sim \Gamma(1, 10^{-3})$, $\lambda_\eta \sim \Gamma(5, 5)$, and $\rho_{\eta k} \sim \text{beta}(1, 0.1), k = 1, \ldots, 3$. Besides, to represent vague prior information about the true values of the calibration parameters, we specify a uniform prior for each component of $\boldsymbol{\theta}$ over $[0, 1]$ (all the prior specifications are the same throughout the paper).

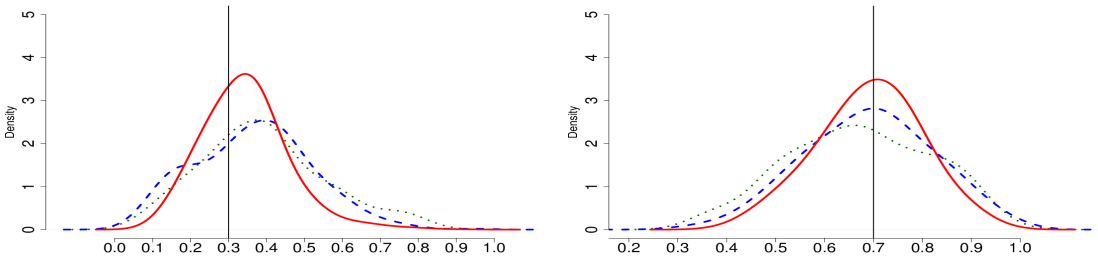

(a) θ_1 (b) θ_2

Figure 2: The posterior densities of θ_1 (a) and θ_2 (b) for Model A (dotted line), B (dashed line) and C (solid line).

The posterior distributions of θ_1 and θ_2 shown in Figure 2(a) and (b). The effect of including SPDE parameters is clearly reflected in a decrease in the bias and the uncertainty in the posterior densities. For Model B, the posterior accuracy of θ_2 is better than Model A, as expected, when the size of the bases of functions is increasing. However, the precision in posterior density is only slightly improved. The posterior density of θ_1 shows a similar patterns between Model A

and B. Additionally, Model C uses fewer coefficients than Model B, while Model C achieves better results in both posterior accuracy and precision. This finding suggests that the calibration can be improved, along with parsimony, by incorporating SPDE parameters in the analysis.

3.2 Example 2: Size issue

Modeling in spatial statistics is usually specified through the covariance function for the data or the latent field. Covariance models for data distributed on the sphere introduce additional constraints in contrast to covariance models for data over an Euclidean space. For example, the issues of choice of distance (great circle or chordal), or the property of positive definiteness of covariance functions on the sphere (Gneiting et al., 2013; Chang et al., 2015). These constraints restrict the choices of covariance structures more on spherical domains than on the plane. Note that Kennedy and O'Hagan (2001) showed that the GP calibration is relatively robust to different covariance structures, so the impact may be modest in some cases.

SHs constitute a frequency-space basis of functions defined on the sphere, which are equivalent to the Fourier series on the spherical domain. Denoting a location $s = (L, l) \in \mathbb{S}^2$ using latitude $L \in [0, \pi]$ and longitude $l \in [0, 2\pi)$, the real SHs function $\psi_{k,h} : \mathbb{S}^2 \to \mathbb{R}$ is defined as

$$\psi_{k,h}(s) = \sqrt{\frac{2k+1}{4\pi}\frac{(k-|h|)!}{(k+|h|)!}} \begin{cases} \sqrt{2}\sin(hl)P_{k,|h|}(\cos L) & \text{if } -k \le h < 0, \\ P_{k,0}(\cos L) & \text{if } h = 0, \\ \sqrt{2}\cos(hl)P_{k,h}(\cos L) & \text{if } 0 < h \le k, \end{cases} \tag{8}$$

where $P_{k,h}$ is the associated Legendre polynomials, the order k determines the frequency of the basis functions over the sphere, and the mode h gives the longitudinal frequency and is generally called the wavenumber in the geophysical literature. Furthermore, the Fourier transform of a GP is still Gaussian (Kirby, 2001). The SHs form a complete set of orthonormal functions in $\mathbb{S}^2$. On the sphere, any square integrable function can thus be expanded as a linear combination of SHs, so SHs are a natural way to represent a function on the sphere.

The second example illustrates the efficiency of the SHs representation for a large spherical output. Given an element $\mathbf{s} = (L, l)$ on the unit sphere, we employ standard spherical coordinates, which can be written as $\tilde{\mathbf{s}} = (\cos(l)\sin(L), \sin(l)\sin(L), \cos(L))$. We create a large dataset embedded in the sphere using a target function defined by

$$f(\tilde{\mathbf{s}}, \theta_1, \theta_2, \theta_3) = \theta_1 s_1^3 + \theta_2 s_1 s_2 + \theta_3 s_3^2, \tag{9}$$

where the true values for $(\theta_1, \theta_2, \theta_3)$ are set to (0.3, 0.7, 0.9). The location input (L, l) is generated on the regular grid $1.9^\circ \times 2.5^\circ$ (to simulate over the same grid as in WACCM), which yields a total of $n = 13,824$ location inputs on the sphere. To investigate the effect of an increase in the number of computer runs on the accuracy of the calibration, we ran $r = 30$ and 60 simulations. The design of the experiments corresponding to the calibration parameters is a maximin LHD. With this design, we tried to cover as much space as possible in the three-dimensional space of the calibration parameters $(\theta_1, \theta_2, \theta_3)$ with 30 and 60 runs, respectively, using the same SH bases to decompose each computer run output, the field surface and the discrepancy. The SH coefficients are estimated by the least squares method. The regression approach can remove at least some of the purely spatial noise (Stein, 2007).

The posterior mean and standard deviation (SD) for $\boldsymbol{\theta}$ calibrated by the 1st to 5th order SH coefficients are presented in the first half of Table 2. Only the 2nd SHs representation can adequately capture the variability of the simulation outputs, and the 3rd order representation gets more precise. Nevertheless, the posterior distributions get worse with higher order representations, due to too many coefficients employed to adequately represent $\boldsymbol{\theta}$ considering the amount of information available. The more computer runs are carried out (60 v. 30), the closer the posterior mean is to the true value under the same order representation. Another important finding is that the higher orders of spherical representations do become helpful when

Table 1: Number of coefficients (N_η) in different orders of the SHs transform, either for the full expansion (F), or for the restricted expansion (R) assuming $h \geq 0$.

Order	1	2	3	4	5	6	7
F	4	9	16	25	36	49	64
R	3	6	10	15	21	28	36

Table 2: The posterior mean and SD of $\boldsymbol{\theta}$ in function (9) under different computer runs and different orders from (a) full or (b) positive analogue part of SHs representation.

(a) Full expansion coefficients ($k \geq h \geq -k$)				
Number of runs	order	$\theta_1$7(=0.3)	$\theta_2(=0.\overline{7})$	θ_3(=0.9)
30	1	0.5196(0.2382)	0.5913(0.2187)	0.8671(0.0773)
	2	0.2699(0.0241)	0.7166(0.0083)	0.8851(0.0141)
	3	0.2693(0.0192)	0.7174(0.0057)	0.8872(0.0084)
	4	0.3807(0.1618)	0.7251(0.0254)	0.9111(0.0564)
	5	0.6119(0.1548)	0.7089(0.0323)	0.7905(0.0837)
60	1	0.4953(0.2375)	0.5996(0.2092)	0.8807(0.0572)
	2	0.2894(0.0035)	0.7094(0.0014)	0.9104(0.0025)
	3	0.2900(0.0025)	0.7094(0.0010)	0.9098(0.0017)
	4	0.3301(0.1028)	0.7193(0.0183)	0.9525(0.0339)
	5	0.5670(0.1699)	0.6829(0.0368)	0.8835(0.0683)
(b) Reduced expansion coefficients ($h \geq 0$)				
Number of runs	order	θ_1(=0.3)	θ_2(=0.7)	θ_3(=0.9)
30	1	0.5237(0.2575)	0.5764(0.2321)	0.8508(0.1031)
	2	0.2716(0.0241)	0.7230(0.0099)	0.8643(0.0229)
	3	0.2698(0.0173)	0.7224(0.0071)	0.8694(0.0167)
	4	0.2763(0.0191)	0.7232(0.0061)	0.8734(0.0164)
	5	0.3248(0.1028)	0.7538(0.0174)	0.8611(0.0544)
60	1	0.5143(0.2401)	0.5897(0.2186)	0.8492(0.0837)
	2	0.2888(0.0052)	0.7105(0.0030)	0.9071(0.0068)
	3	0.2890(0.0032)	0.7103(0.0017)	0.9080(0.0037)
	4	0.2902(0.0025)	0.7096(0.0013)	0.9089(0.0029)
	5	0.2922(0.0037)	0.7084(0.0015)	0.9102(0.0034)

60 runs are carried out. Even so, the improvement achieved by increasing the order eventually reduces.

Because the normalized SH bases with order k and mode h satisfy $\psi^*_{k,h} = (-1)^h \psi_{k,-h}$, where $*$ denotes complex conjugation, then the same order basis with a different sign in the mode h will have a similar periodic structure. A basis with the same order and a different sign for the mode has the same scale and shape properties, except for the shifting in latitude by $\pi/2$. Therefore we can use only the positive analogue of the SH basis to decompose the model outputs. In this approach we can reduce the number of SH coefficients from $N_\eta = (H+1)^2$ to $N_\eta = (H+1)(H+2)/2$ under the H-th order expansion; see Table 1 for a comparison over orders up to 7.

Using the same algorithm and prior specifications, the posterior mean and SD of $\boldsymbol{\theta}$ is presented in the second half of Table 2, using the positive analogue of the SHs representation. These quantities may show, in the lower order expansions, less accuracy than with the complete expansion of the SHs, due to having less coefficients included. But this approach soon catches up in the higher order expansions. For higher orders, the positive analogue representation outperforms the complete expansion of SHs at a much lower computational cost. Indeed, from a statistical point of view, this approach avoids fitting redundant information, and aids identification problems for the calibration parameters.

3.3 Example 3: Comparison with principal components

The third example compares the performance of the SHs representation of the model outputs to that of the PC approach proposed by Higdon et al. (2008). The function with three calibration parameters is set to be

$$f(\tilde{\mathbf{s}}, \boldsymbol{\theta}) = \theta_1 s_1 + \exp(-\theta_2 s_2 - \theta_3 s_3^2), \tag{10}$$

where the true value for $(\theta_1, \theta_2, \theta_3)$ is set to $(0.3, 0.7, 0.9)$. We used locations $(L_i, l_i), i = 1, \ldots, 100$ on a regularly spaced grid. The field surface is $y^F = f(\tilde{\mathbf{s}}, \boldsymbol{\theta}^*) + \epsilon(\tilde{\mathbf{s}})$, where $\epsilon \sim N(0, 0.01)$, and $r = 50$ simulator runs are obtained according to a maximin LHD, denoted by $\boldsymbol{\theta}_j = (\theta_{1j}, \theta_{2j}, \theta_{3j}), j = 1, \ldots, 50$.

The PC based calibration algorithm developed by Higdon et al. (2008) performs a dimensional reduction jointly across the input and output space. This projection is constructed by a data-driven framework (singular value decomposition). The SH representation provides a different approach: it reduces the size of each model output by using the same basis functions to decompose each computer run's output into coefficients; it does not reduce the dimension of the input space. The decomposition is also applied to the observations in order to compare it with the output in the SHs domain.

For the PCs approach, we cannot directly apply the algorithm from Higdon et al. (2008) due to the lack of SH basis functions for the joint input-output projection. Therefore we slightly modify their framework to compare our method with the essential part of their approach. The output surfaces $\boldsymbol{\eta}$ are decomposed by the empirical orthogonal functions (EOFs). EOFs are merely geographically weighted principal components. The EOFs are found by computing the eigenvalues and eigenvectors of a spatially weighted anomaly covariance matrix of a field. The derived eigenvalues provide a measure of the percentage of variance explained by each mode. We calculate the singular value decomposition for the model outputs:

$$\begin{array}{c} \\ s_1 \\ \vdots \\ s_{100} \end{array} \begin{array}{c} \begin{array}{ccc} \theta_1 & \ldots & \theta_{50} \end{array} \\ \begin{pmatrix} \eta_{1,1} & \ldots & \eta_{1,50} \\ \vdots & \ddots & \vdots \\ \eta_{100,1} & \ldots & \eta_{100,50} \end{pmatrix} \end{array} = UDV^T,$$

where the columns of U are the left singular vectors; D has singular values and is diagonal; and V^T has rows that are the right singular vectors. The SVD represents an expansion of the original data in a coordinate system where the covariance matrix is diagonal. The EOFs are then the leading p_η columns of $\frac{1}{\sqrt{r}}UD$.

We retain the first $p_\eta = 10$ EOFs for illustration: the field surface and contour of the first three EOFs for the model output are presented in Figure 3. The cumulative variation explained by the first three components is 71.28%, 82.82% and 92.76%. For the calibration, we also assume that EOF weights are uncorrelated. The GP assumption was imposed on each EOF weight $w_i^P(\mathbf{s}, \boldsymbol{\theta})$ with zero mean, constant variance $1/\lambda_{wi}$ and correlation structure

$$c((i, \boldsymbol{\theta}), (i', \boldsymbol{\theta}'); \rho_{wi}) = \prod_{j=1}^{3} \rho_{wi(j+2)}^{4(\theta_j - \theta_j')^2} \times I_{ii'}. \tag{11}$$

As for the SHs approach, we performed the first five order transforms for the observation and each computer run (see Fig. 4). To illustrate the difference with the EOF approach, we use the 3rd order expansion (16 coefficients) as an example. The SHs transforms the model output as follows

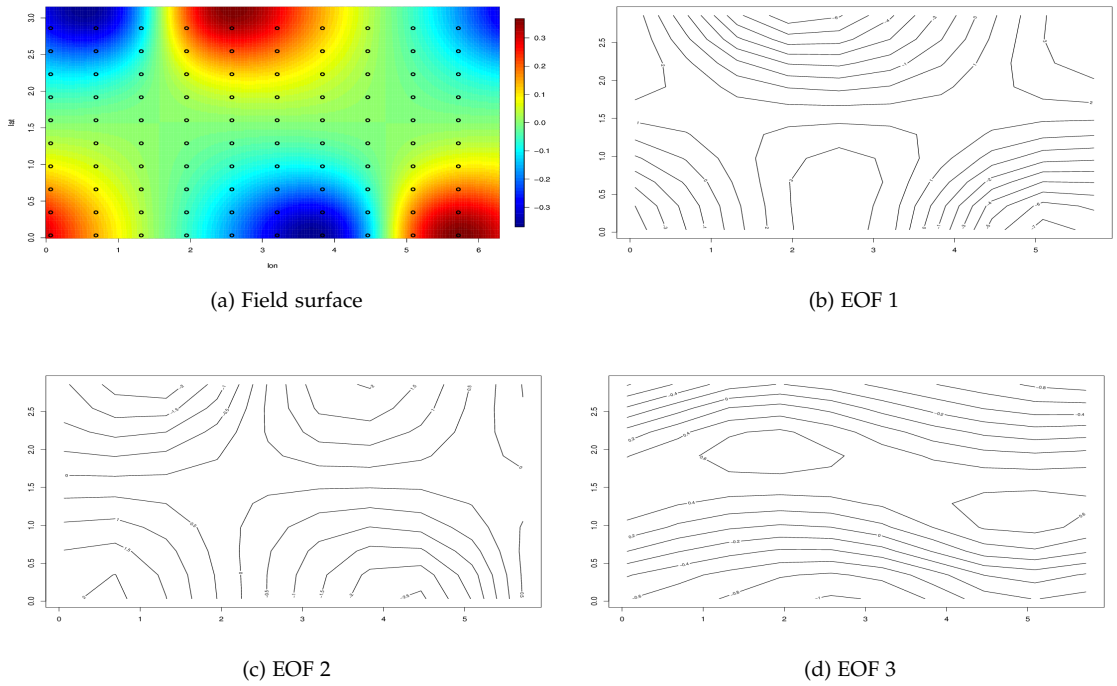

(a) Field surface

(b) EOF 1

(c) EOF 2

(d) EOF 3

Figure 3: Field surface with measurement locations (circles) and first three EOFs.

$$\text{VEC}\left(\begin{pmatrix}\eta_{1,1}\\ \vdots \\ \eta_{100,1}\end{pmatrix};\cdots;\begin{pmatrix}\eta_{1,50}\\ \vdots \\ \eta_{100,50}\end{pmatrix}\right) \rightarrow \text{VEC}\left(\begin{pmatrix}c^M_{1,1}\\ \vdots \\ c^M_{16,1}\end{pmatrix};\cdots;\begin{pmatrix}c^M_{1,50}\\ \vdots \\ c^M_{16,50}\end{pmatrix}\right).$$

Then the model output $\boldsymbol{\eta}$ is transformed into the coefficients $c^M_{k,h}(\boldsymbol{\theta})$, with index $\{k,h\}$ as univariate categorical input and $\boldsymbol{\theta}$ as continuous calibration inputs. The coefficients $\{c^M_{k,h}\}$ obey the GP assumption with mean 0 and covariance structure defined in Equation (1).

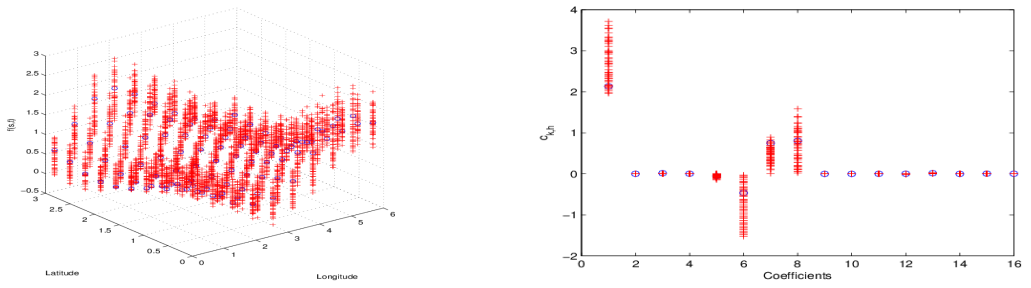

(a) Design on the $\mathbb{S}^2$

(b) Estimated 3rd SH coef.

Figure 4: Field observations (circles) and model output (crosses) on the sphere (a) and estimated 3rd order spherical harmonics coefficients (b).

Table 3: The posterior mean and standard deviation of $\boldsymbol{\theta}$ for the empirical orthogonal functions (EOFs) and spherical harmonics (SHs) approaches.

	components/orders	θ_1(=0.3)	θ_2(=0.7)	θ_3(=0.9)
EOF	1	0.4955(0.2928)	0.5014(0.2905)	0.5088(0.2921)
	2	0.5025(0.2957)	0.4914(0.2909)	0.2957(0.2861)
	3	0.4964(0.2944)	0.5095(0.2811)	0.4983(0.2892)
	4	0.5851(0.3591)	0.4957(0.2212)	0.0274(0.0289)
	5	0.6085(0.3917)	0.6030(0.2754)	0.0612(0.0764)
	6	0.3916(0.3131)	0.7610(0.1462)	0.0600(0.0603)
	7	0.3651(0.3273)	0.6708(0.2099)	0.0427(0.0464)
	8	0.4199(0.3206)	0.6894(0.1644)	0.0341(0.0419)
	9	0.4441(0.3400)	0.5967(0.2020)	0.0387(0.0412)
	10	0.4361(0.3684)	0.5745(0.2312)	0.0345(0.0450)
SH	1	0.4953(0.2875)	0.5996(0.2092)	0.8802(0.0743)
	2	0.2912(0.0077)	0.7126(0.0098)	0.9071(0.0098)
	3	0.2912(0.0054)	0.7126(0.0069)	0.9082(0.0064)
	4	0.3017(0.0627)	0.6878(0.0705)	0.8969(0.0432)
	5	0.2691(0.1160)	0.5958(0.1351)	0.9495(0.0402)

Realizations from the posterior distribution are produced using MCMC. The posterior mean and SD for the calibration parameters are displayed in Table 3. The best estimation of $\boldsymbol{\theta}^*$ in the SHs approach is with the 3rd order representation. The posterior densities approximated by the 4th order representation present higher uncertainties. The EOF approach fails to converge to the true values for the cases of 1 to 10 components. Figure 5 displays the MCMC sample path of the calibration parameters $\boldsymbol{\theta}$ for the 2nd order SHs (9 coefficients) and 9 EOFs representation. We can see that for all calibration parameters in the SHs approach, convergence occurred after roughly 500 iterations, and convergence of the chains can not be established for the EOF approach.

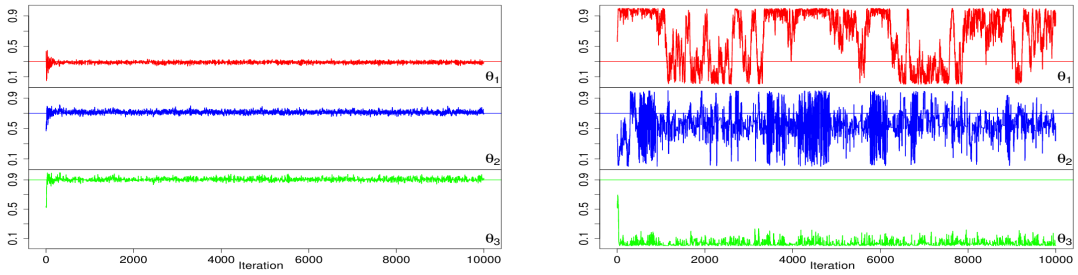

(a) 2nd SHs representation (9 coefficients)

(b) 9 EOFs representation

Figure 5: MCMC paths of $\boldsymbol{\theta}$ for SHs and EOFs algorithms. Solid lines indicate the true values.

The choice of a suitable basis representation is usually highly application dependent. Note that SHs and B–spline are location-dependent basis functions, while PC bases are data driven. The limitation of our technique is that SH representations can only be applied to spatial spherical data, whereas PC decomposition are more widely applicable (but do no acknowledge the nature of the spaces on which it is performed: EOFs do not explicitly account for spatial correlation, only vectorize the spatial outputs). Therefore we can not conclude that the SH basis is always a better choice.

3.4 Example 4: Nonstationary field

We now illustrate how the parameters in an SPDE approach can be incorporated into our calibration algorithm to model nonstationarity over a spherical domain. With 10×10 regularly spaced locations in latitude and longitude and 50 computer runs according to a maximin LHD for the calibration inputs, the function with three calibration parameters is set to

$$f(\tilde{\mathbf{s}}, \boldsymbol{\theta}) = (\frac{1}{2}s_1^2 + \theta_1 s_2 s_3) \times \begin{cases} \theta_2 s_2 & \text{if } L \leq \pi/2 \\ \theta_3 \exp(-s_3 - s_1) & \text{if } L > \pi/2 \end{cases}, \tag{12}$$

where the true values for $(\theta_1, \theta_2, \theta_3)$ are set to $(0.5, 0.2, 0.8)$. We create a nonstationary spatial field by introducing different structures in the Northern and Southern hemispheres, where θ_1 is a global calibration parameter, and (θ_2, θ_3) are local variates, see Fig. 6. First, we performe the SH decomposition onto observations y^F and each computer run $\eta_j, j = 1, \ldots, 50$, and then carry out the calibration on the coefficients $c^F_{k,h}$ and $c^M_{k,h,j}(\theta), j = 1, \ldots, 50$.

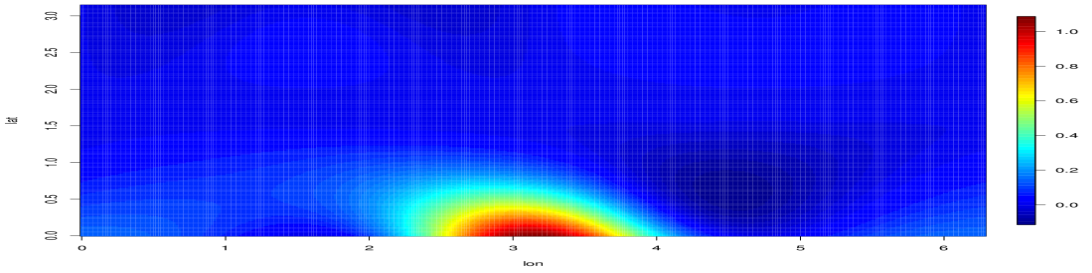

Figure 6: Field surface for function (12).

Here we only use the positive analogue $h > 0$ basis representation. In total, we estimate 13 models with different numbers of expansion order. The results of the analysis of the calibration parameters using the 4th to 7th orders of the SHs representation are shown in the first part of Table 4 (Model A-D). From the results for the posterior sampling, we can see that the global calibration parameter θ_1 is estimated well. However, even though the convergence of an MCMC chain can be established for θ_2 and θ_3, the posterior means are underestimated. Besides, an increase in the order of the expansion does not really improve the results. This underestimation can be viewed as an inability to capture local variations. As $s_2 = \sin(l)\sin(L)$ has stronger variations than $\exp(-s_3 - s_1) = \exp(-\cos(L) - \cos(l)\sin(L))$ (see Fig. 6), those numerical differences also influence the estimation of θ_2 and θ_3.

In order to understand the role of the parameters of the SPDE in the calibration, we first perform a calibration using only the SPDE estimated coefficients $\{\kappa^M, \tau^M\}$. Under the same priors and algorithm, the posterior mean and SD of the first three orders of the expansion for κ^M and τ^M are shown in second part of Table 4 (Model E - G). Even though the calibration does not succeed (and should not without matching original outputs to observations but only SPDE information), the result in the 2nd order expansion for κ^M and τ^M seems informative as the posterior modes are close to the true values. The first two orders of the expansion surface for κ^F and τ^F for the observations y^F are shown in Figure 7. It is difficult to directly interpret the features of $\kappa(s)$ and $\tau(s)$; However, from Figure 7(c) - (d) we can see a strong northeast-southwest flow with high uncertainty (inverse precision) and high correction decay rate over the y^F surface. Besides, the 1st and 3rd order representation results seem unhelpful in detecting the true value of the calibration parameters.

For the next step, we inferred $\{c^M, \kappa^M, \tau^M\}$ jointly with the GP model. We assumed that these three types of coefficients are uncorrelated. Therefore, the covariance matrix in

Table 4: Posterior mean and SD for $(\theta_1, \theta_2, \theta_3)$ in function (12), and number of coefficients (right column) under different orders of expansion for $\{\eta, \kappa, \tau\}$ per model run.

Model	η	κ	τ	θ_1(=0.5)	θ_2(=0.2)	θ_3(=0.8)	$N_\eta + N_\kappa + N_\tau$
A	4	-	-	0.5054(0.0503)	0.1884(0.0479)	0.7620(0.0384)	15
B	5	-	-	0.4975(0.0530)	0.1794(0.0622)	0.7462(0.0499)	21
C	6	-	-	0.4765(0.0619)	0.1664(0.0791)	0.7050(0.0685)	28
D	7	-	-	0.4880(0.1121)	0.1976(0.1265)	0.6954(0.1187)	36
E	-	1	1	0.5793(0.1578)	0.1475(0.0684)	0.6201(0.1997)	6
F	-	2	2	0.5603(0.0969)	0.1887(0.0782)	0.7396(0.0892)	12
G	-	3	3	0.7852(0.0782)	0.4423(0.1554)	0.8581(0.0536)	20
H	4	1	1	0.4516(0.0970)	0.0708(0.0489)	0.4948(0.0367)	21
I	5	1	1	0.4950(0.0438)	0.1331(0.0489)	0.4984(0.0321)	27
J	6	1	1	0.3558(0.0500)	0.1347(0.0521)	0.6855(0.1193)	34
K	4	2	2	0.5532(0.0680)	0.2245(0.1083)	0.7711(0.1094)	27
L	5	2	2	0.5287(0.0676)	0.1785(0.1067)	0.7935(0.0978)	33
M	6	2	2	0.5370(0.0659)	0.1713(0.1098)	0.7894(0.0828)	40

the GP model remains block diagonal. The results of the analyses for the 4th to 6th order representations for the observations and model outputs with the first two orders of expansion with the parameters in the SPDE included are presented in the third part of Table 4. We can see that with the parameters of the SPDE included, we achieve an improvement in the calibration. For example, Model C and K have a similar number of coefficients, but the combination with SPDE increases the estimated accuracy in θ_2 and θ_3. The similar case of Model D and L also supports the use of SPDE information. Model L uses a smaller number of coefficients, while achieving an improvement in terms of increased accuracy in θ_3 and reduced posterior uncertainties. Nevertheless, only in the case of the 2nd order expansion do the SPDE parameters help; the 1st order expansion cannot achieve a good result.

The calibration with the SPDE defined scale and precision parameters did achieve an improvement in terms of increasing the accuracy of the MCMC sampling. However, the impact of the SPDE information has been inconsistent. It also augments uncertainties in the posterior densities in some cases. It is necessary to consider a compromise between estimated accuracy and precision. Besides, in real applications, we often do not know whether the calibrated values work until actually performing a validation. It can be computationally challenging to find the optimized orders for the combination of $\boldsymbol{\eta}$, $\boldsymbol{\kappa}$ and $\boldsymbol{\tau}$.

Similar to most truncated basis representations, we choose the number of basis functions *post hoc*. Our experience can provide model selection criteria as follows: (1) Basis representation for model outputs $\boldsymbol{\eta}$ play a dominant role in the algorithm. The number of basis functions for model outputs (N_η) usually needs to be greater than the total number of basis functions for scale and precision parameters $(N_\kappa + N_\tau)$; (2) Calibration with only one of the coefficients κ or τ cannot improve the analysis. The reason is unclear, but the fact that κ and τ represent a spatial process jointly is tacitly assumed. Recall that the Matérn function is controlled by the smoothness parameter ν, the scale parameter κ, and the precision parameter τ. The smoothness parameter ν is fixed by $\alpha = \nu + d/2$ in connection with the SPDE, therefore the approximated spatial process depends upon κ and τ jointly. Both κ and τ need to be included to reflect the full variation in the spatial field.

3.5 Application to the WACCM experiments

The chemistry–climate model WACCM is a general circulation model of the middle and upper atmosphere. It spans from the Earth's surface to the thermosphere. WACCM provides computer simulations of the Earth's past, present, and future climate states. WACCM is an extension of the National Center for Atmospheric Research Community Earth System Model (CESM).

A series of WACCM runs with compset prescribed sea ice, data ocean and specified

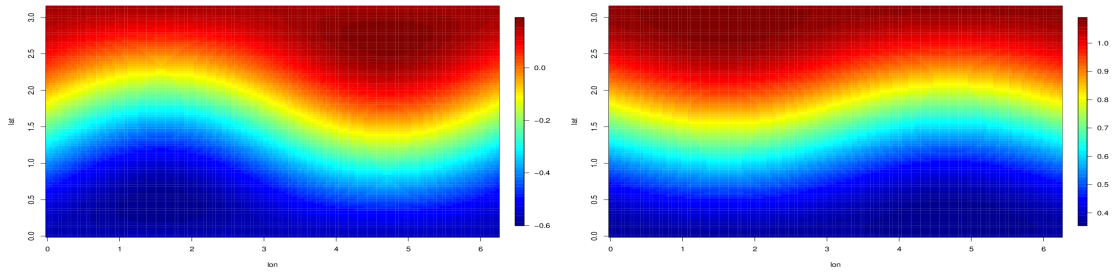

(a) 1st order κ^F

(b) 1st order τ^F

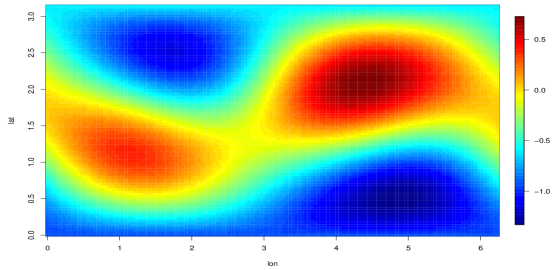

(c) 2nd order κ^F

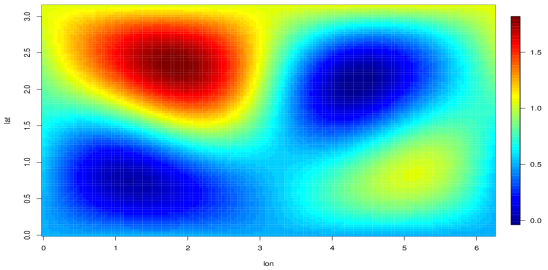

(d) 2nd order τ^F

Figure 7: The first 2 order expansion surface for κ^F and τ^F for observations y^F.

chemistry, with horizontal resolution $1.9 \times 2.5^\circ$ and 66 vertical levels were simulated from 1st January 2000. A run of 2 months takes 3 hours on 16 CPUs on a computer cluster. The GW parameterizations in WACCM depends on four inputs: (1) cbias ($\theta_1 \in [-5, 5]$): anisotropy of the source spectrum, e.g. -5m/s: the spectrum has a stronger westward component, with center of the spectrum at 5m/s westward; (2) effgw ($\theta_2 \in [0.05, 0.3]$): the efficiency factor, measures the gravity wave intermittency; (3) flatgw ($\theta_3 \in [1, 3]$): controls the momentum flux of the parameterized waves at the launch levels; (4) launlvl ($\theta_4 \in [50, 700]$): launch levels of the waves. The value of GW inputs $\boldsymbol{\theta}$ are generated by a maximin LHD. We run $r = 100$ simulations for 2 months. The first month was discarded as a spin–up period. For this study we explore the output of zonal wind at 30mb, February 2000 (an altitude that shows sensitivity to GW parameterizations). Each output has 96 latitudes and 144 longitudes, so the dimension is $n = 96 \times 144 = 13,824$.

To illustrate our methodology, we compare the zonal wind simulations $\boldsymbol{\eta}(\mathbf{s}_i, \boldsymbol{\theta}_j)$, where $\mathbf{s}_i, i = 1, \ldots, 96 \times 144$ are the latitude and longitude on the spherical domain, and $j = 1, \ldots, 100$ is the index of the runs, with outputs from WACCM's standard case, instead of actual observations. Therefore we know the true GW parameters values and can validate our method. Let $\eta^*(\mathbf{s}_i)$ be the zonal wind surface from WACCM standard output. In order to account for possible observation error and lack of physics in the model (discrepancy), we add a smooth noise to $\eta^*(\mathbf{s}_i)$ by assuming that the observations are

$$y^F(\tilde{\mathbf{s}}_i) = \eta^*(\tilde{\mathbf{s}}_i) + \frac{\sigma_{\eta^*}}{5} s_1 + \frac{1}{2} s_2 s_3,$$

where $\tilde{\mathbf{s}}_i = (s_1, s_2, s_3)$ are the spherical coordinates, and $\sigma_{\eta^*} = 11.14$ is the SD of η^*.

Figure 8(c) shows the zonal means calculated over every 5° belt of observations (solid line) and each run of model output (dotted lines). Figure 8(d) represents the grid-by-grid SDs map

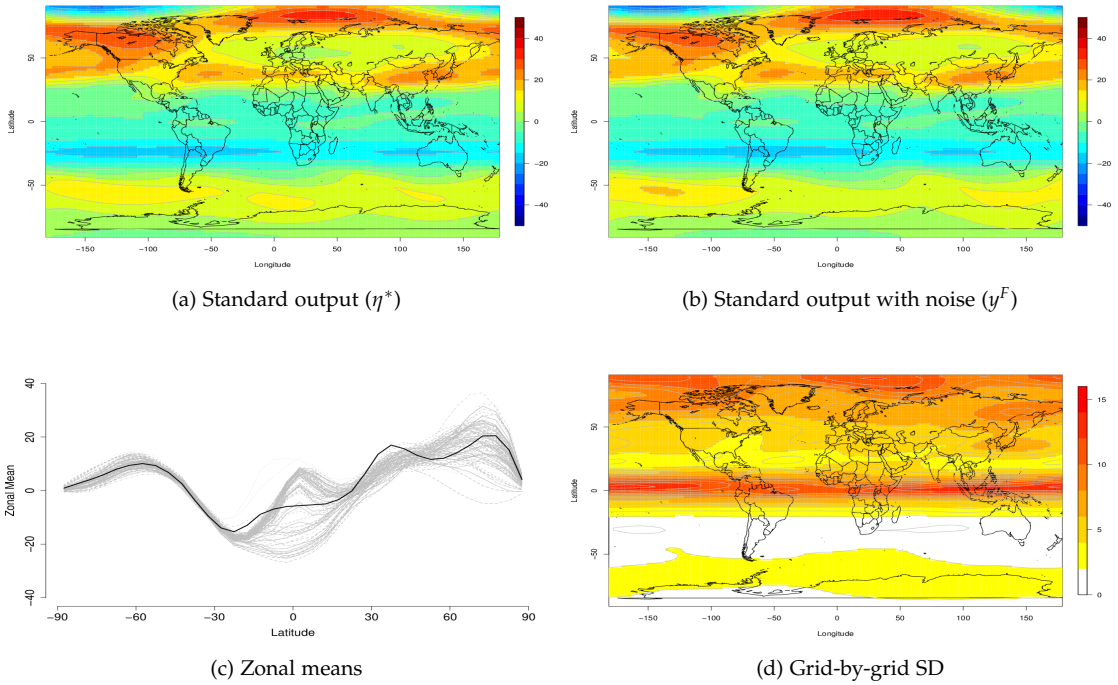

(a) Standard output (η^*)

(b) Standard output with noise (y^F)

(c) Zonal means

(d) Grid-by-grid SD

Figure 8: (a) Zonal wind standard output; (b) Assumed observed surface: noise and discrepancy added to the zonal wind standard output; (c) Zonal means of observations (solid line) and model outputs (dotted lines); (d) Grid-by-Grid SDs map across model runs (30mb, Feb. 2000).

across model outputs. We can see that the spatial process is clearly anisotropic and highly latitude dependent; the uncertainties are concentrated over the North Pole and Tropical regions, and little significant variabilities can be found over the Southern Hemisphere.

For ease of implementation of the MCMC algorithm, we standardize the entire set of responses (observations and WACCM outputs) by the mean and SD of the WACCM zonal wind outputs before performing the SH decomposition. Therefore c^M can be assumed to be mean 0 without loss of generality and the marginal variance in the model outputs is approximately 1. The design space of the calibration parameters is also scaled to be $[0,1]^4$. As for the computational issue, in practice it is difficult to deal with a size of model output beyond moderately large (say $\simeq 2000$). Here we have $r = 100$ computer runs, therefore we seek to decompose each model output with less than 20 coefficients. The results are illustrated by the following 2 models: (1) Model A: 3rd order decomposition in SH bases for model outputs and observations, which yields 10 coefficients for each run; (2) Model B: 3rd order decomposition in SH bases, including 1st order SPDE defined precision and scale parameters, for model outputs and observations, which yields 16 coefficients for each run. As the WACCM simulator produces output on a high resolution regularly spaced grid over a sphere, we construct a spherical triangular mesh by the R–INLA default algorithm without any other particular considerations, and both model outputs and observations share the same mesh.

Figure 9 shows the boxplots of the marginal posterior distributions for the ρ_η's, which control the dependence strength in each pair of $\boldsymbol{\theta}$ in the GP model. The posterior density of ρ_4 closes to 1 that indicate a very weakly significant effect for θ_4. The marginal posterior densities and modes of each calibration parameter are displayed in Fig. 10 and Table 5. From the table we can see that both models calibrate θ_2 well and slightly overestimate θ_4. Both

models underestimate θ_1 significantly, but model B achieves an improvement in terms of increasing the accuracy of the maximum a posteriori estimate. Model B also shows the ability to estimate θ_3, a difficult task as the true value lies on the lower bound. Our approach provides a good compromise between computational feasibility and fidelity to the data by only using parsimonious spherical representations. The results suggest that our technique on calibration of global-scale outputs is effective. The calibration of WACCM with real observations constitute another level of complexity that needs joint scientific and statistical expertise. It is currently under investigation, but is beyond the scope of this paper. Indeed, observations are scarce at these altitudes and show features that require specific understanding of the upper atmosphere dynamics before being used for calibration, and over many years of simulation for adequate comparison.

Table 5: Posterior mode of GW parameters on $[0, 1]$ range for each standardized parameter.

Model	cbias ($\theta_1^* = 0.5$)	effgw ($\theta_2^* = 0.56$)	flatgw ($\theta_3^* = 0$)	launlvl ($\theta_4^* = 0.2308$)
A	0.3613	0.5607	0.2813	0.2818
B	0.4347	0.5473	0.0597	0.2762

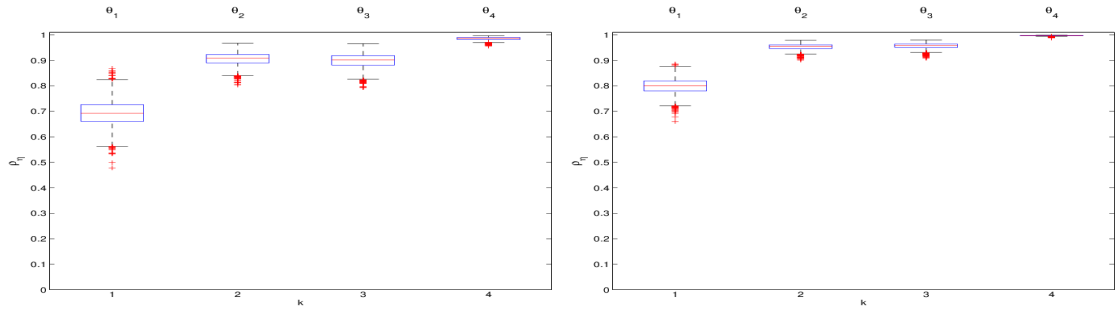

(a) Model A (b) Model B

Figure 9: Boxplots of the marginal posterior distribution for correlation parameters $\boldsymbol{\rho}_\eta$.

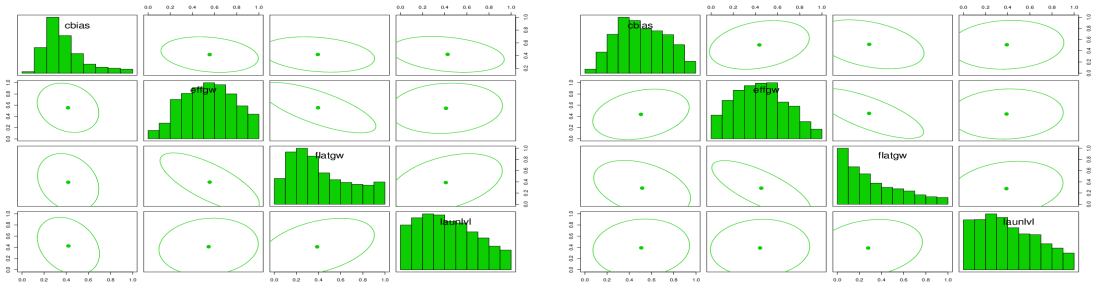

(a) Model A (b) Model B

Figure 10: One and two-dimensional marginals for the posterior distribution of the GW parameters. The off-diagonal panels give the estimated 90% concentration ellipses.

4 Conclusion and discussion

Our approach improved the calibration of large–scale computer model outputs distributed over surfaces, parsimoniously, by using bases representations of the surfaces over the plane or the sphere. In addition, the INLA-SPDE approach was used to decompose its own parameters over the the same bases in order to improve calibration. The synthetic and real examples confirm the ability of our approach to efficiently and accurately perform calibration.

Our method was inspired by the wavelets method of Bayarri et al. (2007), but with a different type of outputs: spatial v. time series. We can expect that the spherical wavelet decomposition may also be a possible alternative basis representation on the spherical domain. But the wavelet transform decomposes a process into different resolutions, and so the correlation between the different resolutions needs to be formalized more carefully.

On the sphere, the SH coefficients represent the wave features at different scales and shapes on the surface. For the purpose of calibration, it is unnecessary to approximate the spatial processes with very high order series expansions of SHs to fit each run of model output best. The critical requirement is to extract sufficient variations behind the SH coefficients about the calibration parameters under a suitable basis representation. However, one may miss important small scale features in lower order of expansion. We also considered data-driven bases representations, such as principal components analysis, which need to seek enough variation for perform an effective analysis; our technique outperforms pricipal component analysis in some settings.

In all these approaches, the choice for the number of basis vectors is currently post hoc. We can check the order of expansion in SHs by detecting the decay rate of coefficients. On the other hand, in case the higher order SHs are required to capture small but meaningful features in a spatial process, one possible solution is to restrict the mode h to a low order in the series expansion of SHs in order to allow more flexibility in variations across latitudes than across longitudes within latitudes (Stein, 2007). The other possibility is to perform a variable selection to those SH coefficients before calibration. For example, in Figure 4(b), it can be seen that not every coefficients show a significant variation. In this case we can expect that the calibration only through the 1st and 5th to 8th coefficients should be able to provide a similar result (all the coefficients decay after 9th coefficient). However, a reliable variable selection technique is required to identify the threshold for the cut-off of redundant coefficients.

Another advantage of using the SH basis is that sequential design is allowed, because the basis elements will not change and model runs are obtained at the same grids or scattered locations. In this study we illustrate our technique to a specific horizontal output from the WACCM simulator. The SHs representation of model outputs can also be extended to time varying processes. As noted by Jones (1963), if a random field on a sphere varies with time, the representation becomes

$$\eta(\mathbf{s}, t) = \sum_{k=0}^{\infty} \sum_{h=-k}^{k} c_{k,h}(t)\psi_{k,h}(\mathbf{s}),$$

where $c_{k,h}(t)$ being an ordinary one-dimensional stochastic process. The set of all $c_{k,h}(t)$ form an infinite dimensional stochastic process. Theoretically we can formulate model outputs in space-time settings with such representations. Nevertheless, in climate or chemistry–transport simulations, we often encounter not only outputs in time and horizontal resolution, but also in vertical resolution. Therefore extensions to 4 dimensional correlations are needed, but they must maintain the computational tractability.

Finally, it is shown that the basic formulation from Kennedy and O'Hagan (2001) can lead to asymptotically inconsistent calibration (Tuo and Wu, 2015a). To improve the Bayesian calibration, we could follow in the future the L_2 calibration in our setting (Tuo and Wu, 2015b).

The benefit would be to yield a better overall match compared to the likelihood distance. This might improve the quality of the calibration further.

References

Bayarri, M., Berger, J., Cafeo, J., Garcia-Donato, G., Liu, F., Palomo, J., Parthasarathy, R., Paulo, R., Sacks, J., and Walsh, D. (2007). Computer model validation with functional output. *The Annals of Statistics*, 35(5):1874–1906.

Bolin, D. and Lindgren, F. (2011). Spatial models generated by nested stochastic partial differential equations, with an application to global ozone mapping. *Annals of Applied Statistics*, 5(1):523–550.

Chang, K.-L., Guillas, S., and Fioletov, V. E. (2015). Spatial mapping of ground-based observations of total ozone. *Atmospheric Measurement Techniques*, 8(10):4487–4505.

Chang, W., Haran, M., Olson, R., Keller, K., et al. (2014). Fast dimension-reduced climate model calibration and the effect of data aggregation. *Annals of Applied Statistics*, 8(2):649–673.

Gneiting, T. et al. (2013). Strictly and non-strictly positive definite functions on spheres. *Bernoulli*, 19(4):1327–1349.

Higdon, D., Gattiker, J., Williams, B., and Rightley, M. (2008). Computer model calibration using high dimensional output. *Journal of the American Statistical Association*, 103:570–5833.

Jones, R. H. (1963). Stochastic processes on a sphere. *Annals of Mathematical Statistics*, 34:213–218.

Jun, M. and Stein, M. L. (2008). Nonstationary covariance models for global data. *Annals of Applied Statistics*, 2:1271–1289.

Kennedy, M. and O'Hagan, A. (2001). Bayesian calibration of computer models. *Journal of the Royal Statistical Society. Series B (Statistical Methodology)*, 63(3):425–464.

Kirby, M. (2001). *Geometric data analysis : an empirical approach to dimensionality reduction and the study of patterns*. Wiley, New York.

Lindgren, F. and Rue, H. (2015). Bayesian spatial and spatiotemporal modelling with R-INLA. *Journal of Statistical Software*, 63(19).

Lindgren, F., Rue, H., and Lindström, J. (2011). An explicit link between Gaussian fields and Gaussian Markov random fields: the stochastic partial differential equation approach. *Journal of the Royal Statistical Society: Series B (Statistical Methodology)*, 73(4):423–498.

Stein, M. L. (2007). Spatial variation of total column ozone on a global scale. *Annals of Applied Statistics*, 1:191–210.

Storlie, C. B., Lane, W. A., Ryan, E. M., Gattiker, J. R., and Higdon, D. M. (2015). Calibration of computational models with categorical parameters and correlated outputs via Bayesian smoothing spline ANOVA. *Journal of the American Statistical Association*, 110(509):68–82.

Tuo, R. and Wu, C. F. J. (2015a). Efficient calibration for imperfect computer models. *forthcoming The Annals of Statistics*.

Tuo, R. and Wu, C. F. J. (2015b). A theoretical framework for calibration in computer models: parameterization, estimation and convergence properties. *submitted*.

Whittle, P. (1963). Stochastic processes in several dimensions. *Bulletins of the International Statistical Institute*, 40:974–994.

Zammit-Mangion, A., Rougier, J., Bamber, J., and Schön, N. (2015). Resolving the Antarctic contribution to sea-level rise: a hierarchical modelling framework. *Environmetrics*, 25(4):245–264.